Overcoming Chiral-Optoelectronic Trade-Off in Two-Dimensional Halide Perovskites for Circularly Polarized Photodetectors

Yarong Gu, Ziqing Li, Ming Deng, Xinyu Zhang, Ying Hu, Li Su, and Xiaosheng Fang**

Two-dimensional (2D) perovskites hold great promise for optoelectronic devices due to the flexible tunability of chiral optical activity and optoelectronic properties. However, the trade-off between strong chiral effect and efficient charge transport restricts their development in high-performance circularly polarized light (CPL) detection. In this work, a tailored achiral-chiral cation mixing strategy is proposed to improve the intermolecular forces and out-of-plane octahedral tilt in the chiral perovskite, which effectively promotes chirality transfer and van der Waals forces tuned vertical growth. Further, a chiral 2D perovskite-based CPL photodetector is constructed with balanced high absorption anisotropy (g_{abs}) and photocurrent anisotropy (g_{Iph}). Compared with materials obtained with pure chiral cations, the maximum g_{abs} of this chiral 2D perovskite increased by 7.33 times. The enhanced chiroptical activity and in-plane transport in vertically oriented chiral 2D perovskites endowed the self-powered CPL device with outstanding performance and a record g_{Iph} of 0.72. This work opens a reasonable paradigm of chiral 2D perovskite photodetectors in information encryption.

1. Introduction

Chiral two-dimensional (2D) perovskites have emerged as promising candidates for high-performance chiral optoelectronic devices such as circularly polarized light (CPL) detectors, chiral light-emitting diodes, and chiral nonlinear optical devices due to the flexible tunability of their organic and inorganic components.[1–3] The inorganic framework of perovskites possesses excellent optoelectronic properties (e.g., tunable bandgap, high charge carrier mobility, high absorption coefficient, and so on), while the chiral cations can introduce unique chiral behaviors, including circular dichroism (CD), nonlinear optical responses, and ferroelectricity.[4–7] Chirality is typically transferred from chiral organic cations to the inorganic framework of perovskites, resulting in chiral 2D perovskites that combine the advantages of chiral materials and 2D layered perovskites. Therefore, it can effectively address the key challenge of integrating high CPL absorption with efficient charge transport in CPL photodetectors.

For chiral perovskite materials, it remains challenging to achieve the trade-off between charge transport performance and chiral selectivity. Due to the rigidity of the inorganic octahedral units,[8] an increase in one side of the conductivity and chirality always causes a decrease in the other. Thus, addressing this issue through rational material design is crucial for the chiral optoelectronic applications of chiral perovskites. Recent studies have explored various strategies aimed at enhancing the performance of chiral perovskites, including designing new chiral organic cations,[9] regulating crystallization,[10] introducing additional dopants,[11,12] or constructing heterostructures.[13,14] Among them, a promising approach is the mixed cation strategy,[15–18] which can construct chiral 2D perovskites with alternating interlayer cations, thereby enhancing material chirality and optimizing stability. However, a lack of universal theoretical frameworks and strategic guidance limits the performance of chiral devices and their further application.

In this work, we introduce a tailored achiral-chiral cation mixing strategy to achieve chirality enhancement of chiral 2D perovskites by reducing interlayer spacing and ordered orientation (Figure S1, Supporting Information). Compared to conventional methods using only single chiral cations, this method significantly increases the chiroptical response of chiral 2D perovskite by 7.33 times. Chiroptical activity characterization combined with crystallographic studies confirms that the reduced interlayer spacing leads to enhanced halogen-halogen interactions between the chiral cations and the inorganic framework, as well as out-

---

Y. Gu, M. Deng, X. Zhang, L. Su, X. Fang
College of Smart Materials and Future Energy
State Key Laboratory of Molecular Engineering of Polymers
Fudan University
Shanghai 200433, P. R. China
E-mail: xshfang@fudan.edu.cn

Z. Li, Y. Hu
State Key Laboratory of Photovoltaic Science and Technology
Shanghai Frontiers Science Research Base of Intelligent Optoelectronics and Perception
College of Future Information
Institute of Optoelectronics
Fudan University
Shanghai 200433, P. R. China
E-mail: lzq@fudan.edu.cn

The ORCID identification number(s) for the author(s) of this article can be found under https://doi.org/10.1002/lpor.202501468

DOI: 10.1002/lpor.202501468

© 2025 Wiley-VCH GmbH

of-plane tilting, promoting the transfer of chirality from the chiral molecules to the inorganic framework. The enhanced chirality and in-plane transport under the specific mixed-cation strategy result in balanced CPL detection performance, where the anisotropy factor of photocurrent surpasses that of state-of-the-art chiral 2D perovskite-based self-powered CPL detectors. This work contributes to a fundamental understanding of the mechanism of chirality transfer in chiral perovskites and demonstrates a paradigm for developing applications based on highly sensitive chiral perovskites for CPL.

2. Results and Discussion

2.1. Strong Chiral Effect in 2D Perovskite Induced by Tailored Achiral-Chiral Cations

The rational design of cation layers plays a crucial role in synthesizing 2D perovskites with a strong chiral effect and enhancing the understanding of the chiral transfer mechanisms. As shown in **Figure** 1a, the $[PbI_6]^{4-}$ octahedral layers, which share corners within the 2D chiral perovskite structure, are sandwiched between two layers of chiral organic chains. These fundamental units are interconnected through van der Waals forces. The selection of cations significantly influences the crystal interlayer distance, which in turn affects halogen-halogen interactions and alters the out-of-plane tilting of the octahedra that is linked to chirality. To modulate chirality in 2D perovskites, we devise a tailored achiral-chiral cations strategy, in which (R/S)-1-(3-bromphenyl)-ethylamine (R-/S-3BrMBA) cation, containing additional halogens, serves as the chiral cation, and phenylethylammonium (PEA) cation is selected as an achiral cation. Calculations of van der Waals radius reveal that the molecular radii of chiral cation and achiral cation are 3.798 and 3.288 Å (Figure 1b), respectively. Therefore, achiral cations with a smaller molecular length possess less steric hindrance, which can lead to an enhanced interaction between the cation and the inorganic framework while reducing the van der Waals gap between the two organic layers.

Under the specific conditions of PEA^+:R-/S-$3BrMBA^+$ = 1:3 (molar ratio), $(R\text{-}3BrMBA_{0.75}PEA_{0.25})_2PbI_4$ and $(S\text{-}3BrMBA_{0.75}PEA_{0.25})_2PbI_4$ (denoted as R1 and S1, respectively) enantiomers are successfully synthesized. The X-ray diffraction (XRD, Figure 1c) patterns show an excellent agreement with the simulated XRD based on the corresponding single crystal structures, indicating high crystallinity of R1 and S1. And the peak at $2\theta = 6.4°$ corresponds to the secondary phase.[19] Top-view field emission scanning electron microscopy (FESEM, Figure S2, Supporting Information) images reveal a smooth and uniform surface. The differential absorption of left-handed circularly polarized light (LCPL) and right-handed circularly polarized light (RCPL) by the chiral perovskites is investigated through CD spectroscopy. Notably, the CD spectral profiles of R1 and S1 are markedly distinct from those of R-/S-3BrMBA, with their CD signals primarily located in the ultraviolet region (Figure S3, Supporting Information). R1 and S1 display mirror-image CD signals correlating with their respective absorption peaks (Figure 1d). At the exciton absorption peak corresponding to 495 nm (Figure 1e), the positive CD signal of R1 indicates that LCPL has preferential absorption, whereas S1 exhibits the opposite behavior, favoring RCPL. This phenomenon, known as the Cotton effect, arises from electronic transitions within excitonic bands induced by the presence of chiral cations.[15,20,21] This indicates the successful transfer of chirality from the chiral organic amine to the entire perovskite structure. To distinguish genuine chiral-induced CD from artifacts caused by macroscopic anisotropy, we used the R1 thin film as a representative sample and performed CD measurements on both the front (air-facing) and back (substrate-facing) sides of the R1 thin film under identical conditions. Critically, the CD spectra from both sides exhibit nearly identical intensity and sign (Figure S4a, Supporting Information), while the contribution of linear dichroism and linear birefringence (LDLB) was negligible (Figure S4b, Supporting Information). This confirms that the observed signals originate from intrinsic chirality rather than linear dichroism or birefringence effects. To quantify the degree of CPL absorption, the absorption anisotropy factor (g_{abs}) is calculated using the following equation:[22]

$$g_{abs} = \frac{CD\left(mdeg\right)}{32980 \times Absorbance} \tag{1}$$

As shown in Figure S5 (Supporting Information), the maximum g_{abs} of R1 and S1 are 2.2×10^{-3} and 1.8×10^{-3}, respectively, which are of the same order of magnitude as most reported advanced chiral perovskites.[15,23–26] This suggests that they are promising candidates for CPL detection. Furthermore, the difference in maximum g_{abs} between R1 and S1 primarily arises from the inherent structural and electronic differences between the R- and S-enantiomers in chiral perovskite systems.[27,28] Figure 1f depicts the crystal structure of R1, which crystallized in the chiral space group of $P2_1$, further confirming the chiral transfer of chiral organic amine to the perovskite structure. Additional crystallographic information can be found in Table S1 (Supporting Information).

2.2. Promoted Chirality Transfer via Intermolecular Forces and Octahedral Tilt

To investigate the manipulation mechanism of chirality through the introduction of an achiral cation, we synthesize R-type chiral perovskites with varying achiral cation contents while maintaining a constant molar ratio of organic cations to lead halides. According to the proportion of achiral cations in the organic cations mixture (0, 0.25, 0.5, 0.75, and 1, details are shown in Table S2, Supporting Information), the samples are denoted as R0, R1, R2, R3, and R4, respectively. It can be seen from the CD spectra (**Figure** 2a; Figure S6, Supporting Information) that R1 shows the strongest CD signal, while R3 and R4 do not show any CD response. At the same time, with increasing achiral cation content, the absorption peak of the corresponding mixed cations perovskites undergoes red shifts, accompanied by decreases in bandgap (Figures 2b; Figure S7, Supporting Information). The calculated maximum g_{abs} for each sample are presented in Figure 2c. Obviously, R1, prepared at a molar ratio of 1:3, exhibits the highest maximum g_{abs}. The maximum g_{abs} of R1 reach 2.2×10^{-3}, which is 7.33 times greater than that of R0 (3×10^{-4}) obtained with pure chiral cations. However, when the amount of achiral cation is further increased to the molar ratio

18638899, 2025, 24, Downloaded from https://onlinelibrary.wiley.com/doi/10.1002/lpor.202501468 by Fudan University, Wiley Online Library on [09/03/2026]. See the Terms and Conditions (https://onlinelibrary.wiley.com/terms-and-conditions) on Wiley Online Library for rules of use; OA articles are governed by the applicable Creative Commons License

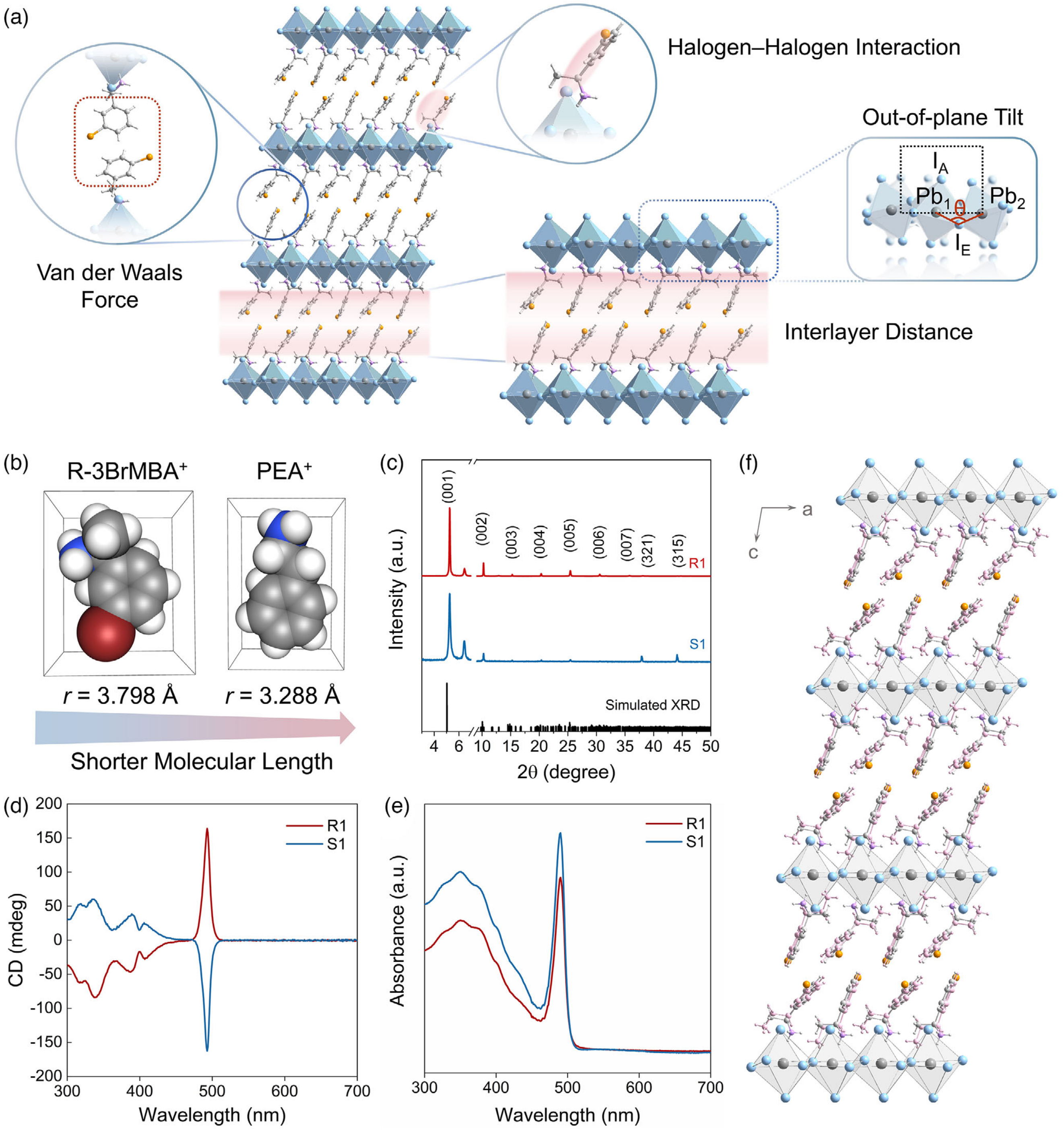

Figure 1. Tailored achiral-chiral cation 2D perovskites. a) Schematic illustration of the cation-altered intermolecular forces and crystal structures in chiral 2D perovskites. b) Van der Waals sphere models and calculated van der Waals radii of R-3BrMBA$^+$ and PEA$^+$. c) XRD patterns of R1 and S1, and simulated XRD pattern of R1 single crystal. d) CD spectra of R1 and S1. e) Absorption spectra of R1 and S1. f) The crystal structure of R1 viewed along the b axis.

of 1:1, there is a decline in g_{abs} for R2 (1.6×10^{-5}). To elucidate the origin of the observed chiroptical activity, the degree of lattice distortion is statistically estimated by XRD (Figure 2d). The shift of the main peak (001) to high angles and the widening of the full width at half maximum (FWHM) indicate a decrease in the interlayer spacing and an increase in the lattice distortion.[29] Note that the FWHM of R0 is smaller than that of R1, while the g_{abs} of R1 is 7.33 times greater than those of R0. This leads to the interesting question of why the tailored achiral-chiral cations can achieve such a strong chiral effect.

© 2025 Wiley-VCH GmbH

18638899, 2025, 24, Downloaded from https://onlinelibrary.wiley.com/doi/10.1002/lpor.202501468 by Fudan University, Wiley Online Library on [09/03/2026]. See the Terms and Conditions (https://onlinelibrary.wiley.com/terms-and-conditions) on Wiley Online Library for rules of use; OA articles are governed by the applicable Creative Commons License

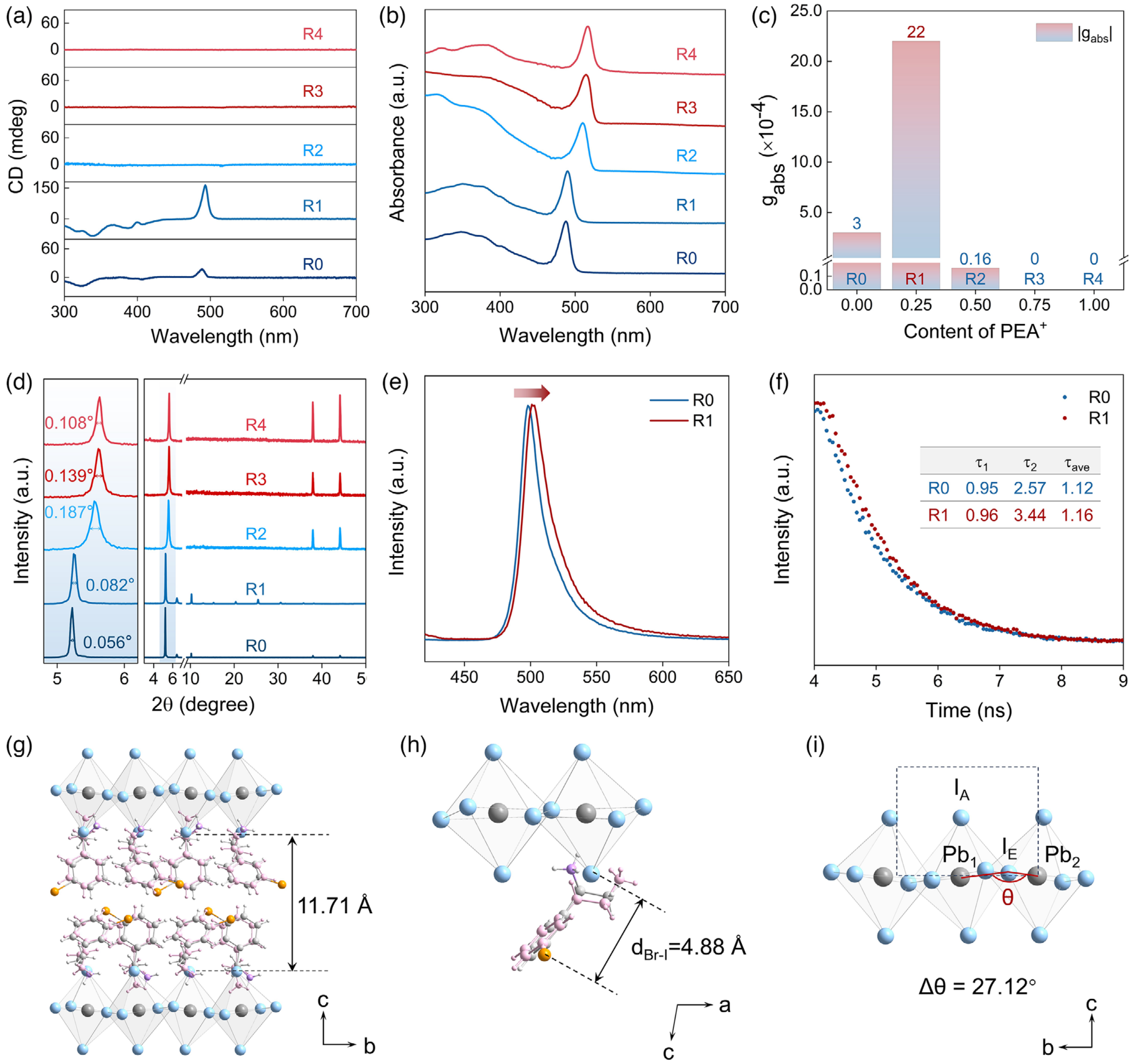

	τ_1	τ_2	τ_{ave}
R0	0.95	2.57	1.12
R1	0.96	3.44	1.16

Figure 2. Chiral manipulation of 2D perovskites by achiral cations. a–d) Characterization of R-type chiral perovskites with different PEA$^+$ contents. (a) CD spectra, (b) Absorption spectra, (c) Summary of maximum g_{abs} values, (d) XRD patterns. e) PL spectra of R0 and R1. f) PL decay curves of R0 and R1. g–i) Intermolecular forces and structural description. Interlayer spacings (g), halogen-halogen interactions (h), and out-of-plane tilt (i) for R1. I_E denotes the apical iodine atom that links two lead atoms (Pb(1) and Pb(2)) within the octahedral framework.

Therefore, we use R0, that composed of pure chiral cations as a reference to further study the underlying reasons for the enhanced chirality in R1. The photoluminescence (PL) properties of 2D perovskites are highly sensitive to distortions in the inorganic framework. As shown in Figure 2e,f the red shift of the PL peak and the increase of the PL lifetime further confirm that R1 mixed with a specific achiral cation has a smaller interlayer spacing and an increased distorted structure.[30,31] It indicates that the enhanced chirality may originate from the increased intermolecular forces and structural distortion within the inorganic framework. To validate this hypothesis, the crystal structure and crystallographic parameters of R1 and R0 are determined by single crystal XRD (Figure S8 and Tables S1–S4, Supporting Information). As depicted in Figure 2g and Figure S9a (Supporting Information), the interlayer spacings of R1 and R0 are 11.71 and 11.81 Å, respectively. The reduced interlayer spacing shortens the minimum distance between the Br atoms of the chiral cations in R1 and the I atoms of the inorganic octahedron, inducing a stronger halogen-halogen interaction (Figure 2h and Figure S9b, Supporting Information). This is further supported by the blue shift of the peak associated with the stretching vibration of the C—Br bond in the Fourier Transform infrared (FT-IR) spectra

© 2025 Wiley-VCH GmbH

18638899, 2025, 24, Downloaded from https://onlinelibrary.wiley.com/doi/10.1002/lpor.202501468 by Fudan University, Wiley Online Library on [09/03/2026]. See the Terms and Conditions (https://onlinelibrary.wiley.com/terms-and-conditions) on Wiley Online Library for rules of use; OA articles are governed by the applicable Creative Commons License

(Figure S10, Supporting Information). The C—Br bond in R0 exhibits a stretching vibration at 1064 cm^{-1}, while in R1, it appears at 1067 cm^{-1}.[32] The Br—I bond increases the effective charge on carbon and reduces the corresponding force constant of the C—I bond, thereby explaining the observed blue shift in the FT-IR spectra.[33] The blue shift observed in the FT-IR peak center aligns consistently with other evidence from the XRD main peak shift to higher angles, absorption/PL peak red shift, and crystallographic data. These results collectively indicate reduced interlayer spacing and enhanced halogen-halogen interactions in R1. This enhanced halogen-halogen interaction facilitates the chirality transfer of the chiral cation to the inorganic framework.[9] Furthermore, the out-of-plane tilt angle $\Delta\theta = 180° - \theta$ is used to evaluate inter-octahedral distortion, where θ represents the $\text{Pb}_1\text{-I}_\text{E}\text{-Pb}_2$ bond angle[34] and I_E denotes the apical iodine atom that links two lead atoms (Pb(1) and Pb(2)) within the octahedral framework. The measured $\Delta\theta$ for R1 is 27.12° (Figure 2i), which is significantly larger than that of R0 (26.33°, Figure S9c, Supporting Information), indicating an increased out-of-plane tilt in R1. It is evident that the intensified halogen-halogen interactions promote the distortion of the inorganic framework, contributing to the enhanced chirality.

2.3. Oriented Vertical Growth Tuned by Van Der Waals Forces

Notably, specific achiral-chiral cations also tune film growth. According to the Bragg-Brentano diffraction geometry, the XRD diffraction intensity corresponds to the out-of-plane orientation of a particular lattice plane.[35] Figure S11 (Supporting Information) shows that the diffraction intensity of the (001) crystal plane of R1 is significantly enhanced, indicating that achiral cations effectively regulate film crystallization. Furthermore, we use grazing incidence wide-angle X-ray scattering (GIWAXS) characterization at incident angles of 0.1°, 0.2°, and 0.4° to investigate the structural changes in R0 (**Figure** 3a–c) and R1 (Figure 3d–f) from the surface to the interior. It can be observed that R1 exhibits clearer diffraction points, along with a reduced distribution of parallel orientations and a significantly enhanced intensity of vertical orientations, suggesting that the lattice predominantly orients perpendicular to the substrate.[36–38] Additionally, no new diffraction points appear in R1 at varying incident angles, indicating consistent orientation across different depths. These results demonstrate that R1 has more ordered directional growth compared to R0.

Based on the above studies, a detailed crystallization model of 2D chiral perovskite films can be constructed. Initially, the powder sample is pre-synthesized as a precursor via a solvothermal method, which is then redissolved to yield a precursor solution containing large polyiodide colloids at high concentration[39] (Figure S12, Supporting Information). This effect is particularly significant in R1 with the incorporation of achiral cations. Dynamic light scattering (DLS) studies revealed particle size distributions for the precursor of R0 and R1 (Figure S13, Supporting Information), with average sizes of ≈1.451 and 4.934 nm, respectively. The reduced steric hindrance associated with the smaller achiral cation (Figure 1b) facilitates enhanced binding energy between the organic chains and inorganic octahedra. Consequently, this leads to improved crystallization quality and chiral transfer efficiency, which is corroborated by our systematic study above.

Specifically, enhanced diffraction intensity in XRD (Figure S11, Supporting Information), increased fluorescence lifetime in TRPL (Figure 2f), and distinct diffraction points in GIWAXS (Figure 3d–f) suggest improved crystallization quality. Additionally, the amplified CD signal (Figure 2a) and the increase of g_abs (Figure 2c) confirm effective chirality transfer. Moreover, during the film formation process, these large-sized colloids can function as crystal nuclei that promote heterogeneous nucleation, forming a 2D layered structure through van der Waals forces between organic chains (Figure 3g). Structural analysis reveals that the van der Waals gap of R1 (3.84 Å) is significantly smaller than that of R0 (4.39 Å), which promotes the oriented growth of R1. Unlike typical 2D perovskites that are usually known to adopt horizontal structures (Figure S14, Supporting Information), our chiral 2D perovskites form vertical structures due to the unique crystallization kinetics of hot casting. (see the Device fabrication section of Supporting Information for details).[40] This enhanced film orientation is expected to facilitate the directional transport of photogenerated charge carriers between electrodes, thereby increasing the photocurrent of the device.

2.4. High Asymmetry Factor of Photocurrent Achieved in CPL Detection

To maximize the resolution of CPL, R1 is selected as the CPL-sensitive layer. A vertical CPL detector is subsequently designed with a device architecture consisting of FTO/PEDOT:PSS/perovskites/PC_{71}BM/Ag, as illustrated in **Figure** 4a. Figure S15 (Supporting Information) presents a cross-sectional FE-SEM image of the constructed CPL detector layered structure. A smooth and continuous film can be observed, which is conducive to balanced light absorption and charge transfer.[41] The photocurrent response and stability of the device are assessed through cyclic on/off switching. And Figure 4b shows the current-time curve and repeated light-switching behavior of the device under 0 V bias and 490 nm illumination. The device exhibits a photocurrent of up to 2.5 μA, characterized by a regular switching curve with no observed decrease in photocurrent. Responsivity (R_λ) and detectivity (D^*) are critical parameters for evaluating the photoelectronic conversion capability of photodetectors, as defined by the following equation:[42–44]

$$R_\lambda = \frac{I_{photo} - I_{dark}}{P_\lambda \cdot S} \tag{2}$$

$$D^* = \frac{R_\lambda}{\sqrt{\frac{2eI_\text{dark}}{S}}} \tag{3}$$

where I_photo and I_dark represent the photocurrent and dark current, P_λ is the light power density at a particular wavelength (λ), S is the effective illumination area of the device, and e is the electron charge. As shown in Figure 4c, the device attains maximum R_λ and D^* of 66 mA W^{-1} and 3×10^{11} Jones under 0 V bias, comparable to the reported chiral perovskite-based self-powered CPL detectors (detailed comparisons are shown in Table S4, Supporting Information). The photocurrent increases steadily with

© 2025 Wiley-VCH GmbH

18638899, 2025, 24, Downloaded from https://onlinelibrary.wiley.com/doi/10.1002/lpor.202501468 by Fudan University, Wiley Online Library on [09/03/2026]. See the Terms and Conditions (https://onlinelibrary.wiley.com/terms-and-conditions) on Wiley Online Library for rules of use; OA articles are governed by the applicable Creative Commons License

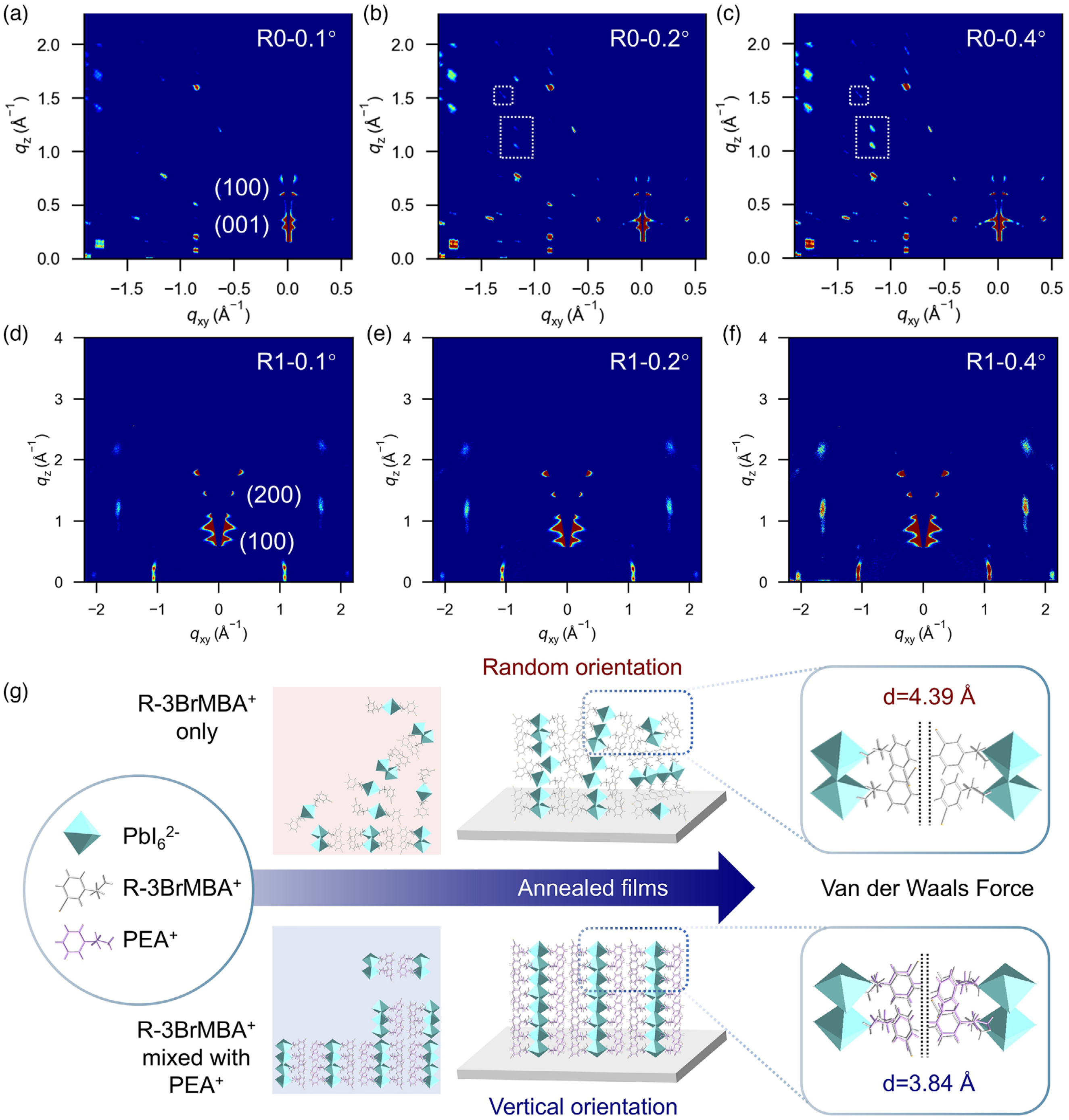

Figure 3. Van der Waals force-assisted oriented film-formation process. a–c) GIWAXS patterns of R0 films with incident angles of 0.1° (a), 0.2° (b), and 0.4° (c). d–f) GIWAXS patterns of R1 films with incident angles of 0.1° (d), 0.2° (e), 0.4° (f). g) Schematic illustration of the van der Waals force-assisted oriented film-formation process of the tailored achiral-chiral cations 2D perovskites.

increasing optical power density (Figure 4d), indicating a direct proportionality between the number of photogenerated carriers and the absorbed photon flux. The dependence of the photocurrent on light power density follows the power law described by[45]

$$I = \alpha P^{\theta} \tag{4}$$

where α represents a constant of light wavelength, and the index θ determines the photocurrent response to the light power density. The fitting curve derived from this relationship in Figure 4d exhibits linear behavior with $\theta = 0.86$. The θ closed to 1 implies that fewer carriers recombine during the complex processes of electron-hole pair transport (generation, trapping, separation, and recombination) in the device, which eventually fa-

18638899, 2025, 24, Downloaded from https://onlinelibrary.wiley.com/doi/10.1002/lpor.202501468 by Fudan University, Wiley Online Library on [09/03/2026]. See the Terms and Conditions (https://onlinelibrary.wiley.com/terms-and-conditions) on Wiley Online Library for rules of use; OA articles are governed by the applicable Creative Commons License

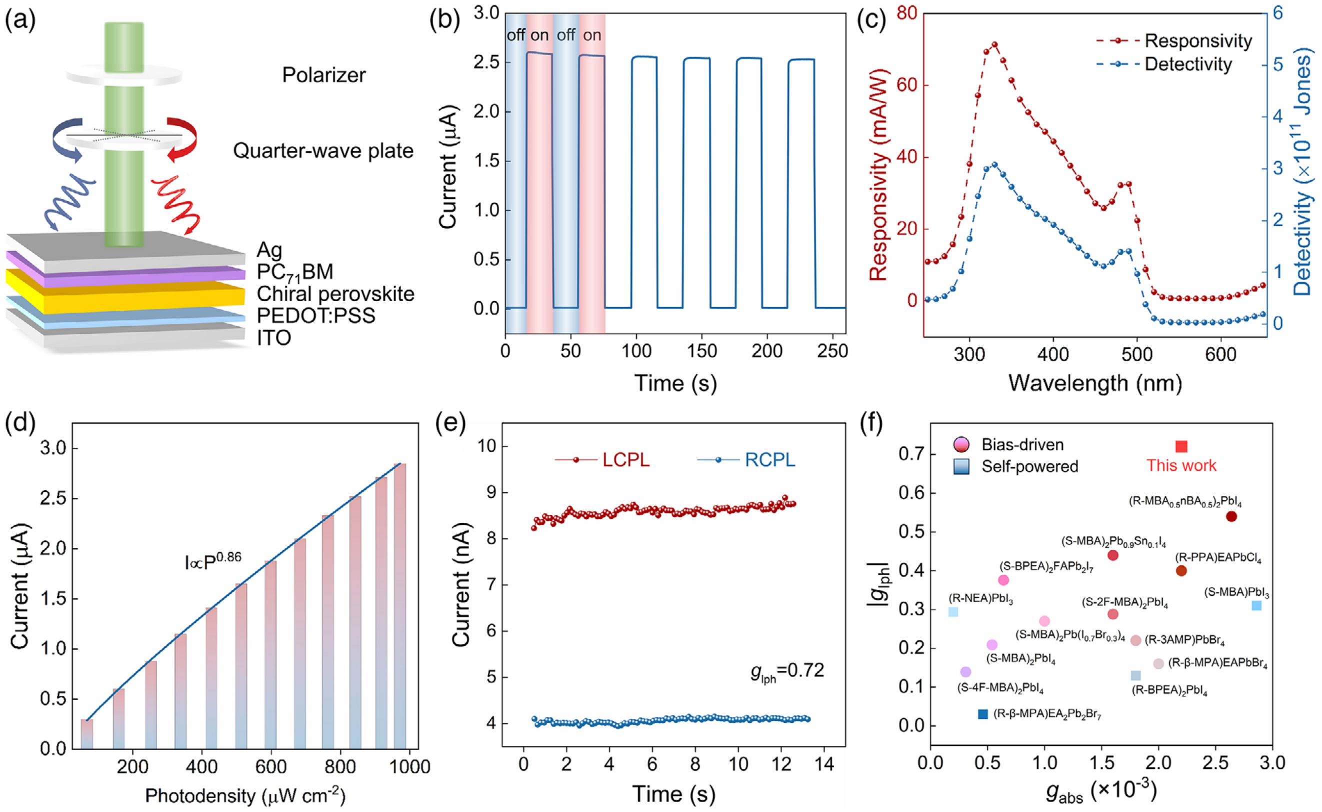

Figure 4. Chiral 2D perovskite-based CPL photodetectors. a) Device configuration. b) Time-dependent reproducible photocurrent on/off switching at 0 V bias. c) Light intensity-dependent detectivity and responsivity of R1 at 0 V bias. d) Corresponding fitting curves for the relationship between the photocurrent and the light intensity. e) The current-time curves under LCPL and RCPL at 0 V bias. f) g_{abs} and $|g_{Iph}|$ in reported studies for chiral perovskite-based CPL photodetectors (details are shown in Table S5, Supporting Information).

vors the increase of photocurrent.[46] Temporal response measurements of R0- and R1-based CPL detectors (Figure S16, Supporting Information) quantified the rise time (τ_r) and decay time (τ_d), defined as the durations for photocurrent to rise from 10% to 90% and fall from 90% to 10% of maximum current, respectively. Compared to the R0-based detector, the R1-based device achieves significantly faster response times, demonstrating a reduced τ_r from <0.96 s to <0.475 s and a shortened τ_d from <0.84 s to <0.620 s.

Encouraged by these promising results, we subsequently focused on investigating the capability of the chiral perovskite-based photodetectors to distinguish between LCPL and RCPL. A polarizer and a quarter-wave plate are introduced into the incident light path, generating LCPL and RCPL by rotating the quarter-wave plate to 135° and 45°, respectively. Notably, artifacts arising during CPL illumination for CPL photodetector characterization may compromise the reliability of CPL discrimination metrics.[47] To exclude and verify these issues, we implemented systematic protocols to eliminate potential artifacts caused by the polarization purity of the light source, environmental fluctuations, and intrinsic anisotropy of the sample during the CPL photodetection process (see the Material characterization and optoelectronic measurements section of Supporting Information for details). As shown in Figure 4e, the photocurrent under the illumination of LCPL and RCPL (I_{LCPL} and I_{RCPL}) at 3.88 mW cm^{-2} is measured to be 8.5 and 4 nA, respectively. Analogous to the g_{abs}, the anisotropy factor of photocurrent (g_{Iph}) is defined as follows to quantitatively evaluate the distinguishability of CPL:[48]

$$g_{Iph} = \frac{2 \times \left(I_{LCPL} - I_{RCPL} \right)}{I_{LCPL} + I_{RCPL}} \tag{5}$$

notably, the g_{Iph} is calculated to be 0.72 under 0 V bias, achieving an unprecedented level for self-powered CPL detection based on chiral 2D perovskites. Figure 4f compares g_{abs} and $|g_{Iph}|$ in reported studies for CPL photodetectors based on different chiral perovskites (details are shown in Table S5, Supporting Information). In contrast, our device achieves superior g_{abs} and the highest g_{Iph}, underscoring the critical role of the tailored achiral-chiral cations strategy in enhancing chiroptical response through efficient chirality transfer. Clearly, such a remarkable CPL detection ability is not only related to g_{abs}, given that g_{Iph} exceeds g_{abs}. First, given that the high g_{abs} of R1, it efficiently generates different spin polarized carriers under RCPL and LCPL illumination. The photocurrent in the CPL photodetector exhibits anisotropy (g_{Iph}) that depends not only on spin-polarized carrier generation but also on spin-dependent charge transport and collection.[49] The spin-selectivity in charge transport arises from the chiral-induced spin selectivity (CISS) mechanism, wherein the R1 layer functions as an in situ spin filter.[50] The chirality of R1 preferentially transmits carriers with one spin state while suppressing those with the opposite spin state. Furthermore, the specific ver-

© 2025 Wiley-VCH GmbH

18638899, 2025, 24, Downloaded from https://onlinelibrary.wiley.com/doi/10.1002/lpor.202501468 by Fudan University, Wiley Online Library on [09/03/2026]. See the Terms and Conditions (https://onlinelibrary.wiley.com/terms-and-conditions) on Wiley Online Library for rules of use; OA articles are governed by the applicable Creative Commons License

18638899, 2025, 24, Downloaded from https://onlinelibrary.wiley.com/doi/10.1002/lpor.202501468 by Fudan University, Wiley Online Library on [09/03/2026]. See the Terms and Conditions (https://onlinelibrary.wiley.com/terms-and-conditions) on Wiley Online Library for rules of use; OA articles are governed by the applicable Creative Commons License

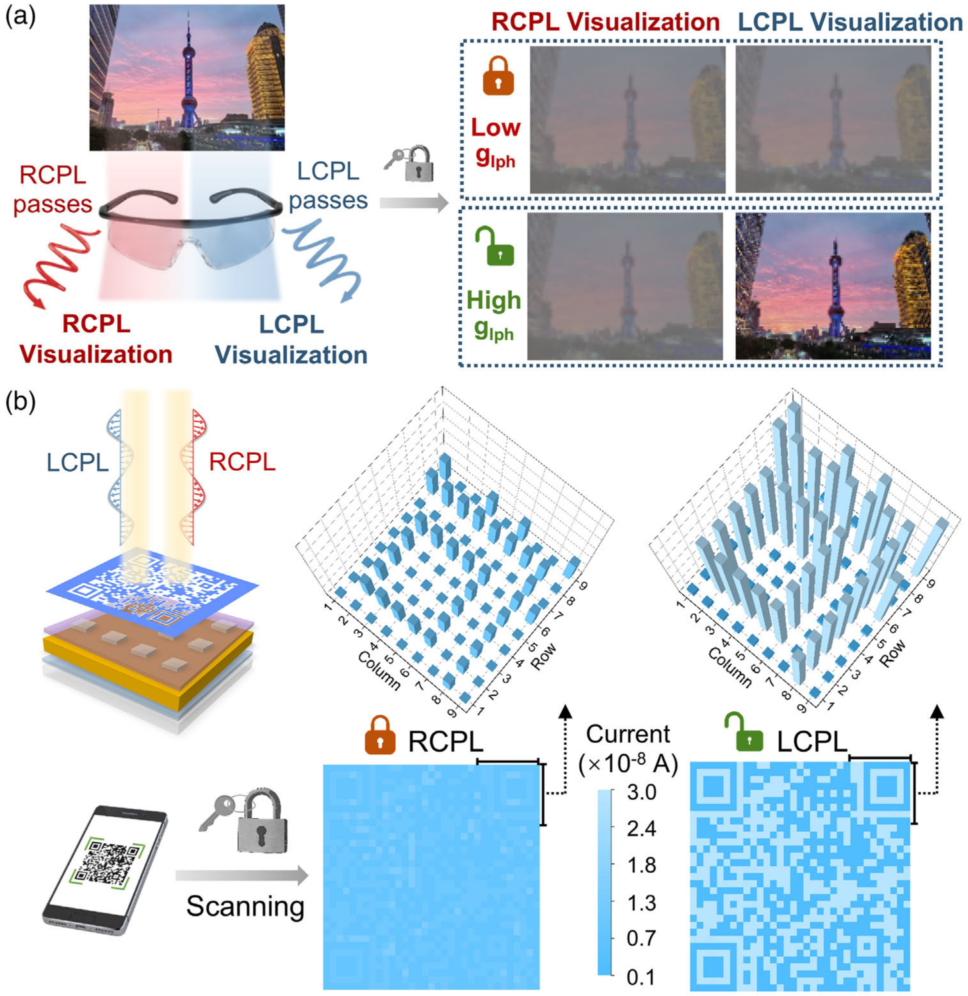

Figure 5. CPL imaging for information encryption. a) Schematic illustration of CPL imaging encryption principle. b) Proof-of-concept encrypted QR code imaging of the device. The QR code mask is projected onto the device under LCPL and RCPL illumination, respectively. The 2D current map is obtained by extracting the photocurrent value, and the concealed QR code image is fully inspected and can be directly read by a smartphone. This QR code links to our research group's website.

tical orientation endows R1 with better in-plane charge transport, thereby inducing the circular photogalvanic effect (CPGE)[51] and improving the efficiency of photocarrier injection from R1 to the electrode.[29] These combined mechanisms ultimately lead to CPL-dependent differential photocurrent responses.

2.5. Encrypted CPL Imaging Achieved by High Giph

Objects composed of different materials typically reflect or scatter polarized light in distinct ways when exposed to natural light.[52] Therefore, the ability to distinguish CPL is crucial for object recognition under illumination, particularly for target detection in complex scenarios like anti-camouflage and anti-interference. Considering the high g_{Iph} of the achiral-chiral cation perovskite CPL detector, we employ this detector to extract CPL image encryption information. The principle of CPL imaging encryption is illustrated in **Figure** 5a. At low g_{Iph}, the contrast between the visualizations of RCPL and LCPL is minimal, making it challenging to extract effective information. However, high g_{Iph} enables high-fidelity visualization with excellent resolution, facilitating effective information transmission. To bolster the security of information transfer, we design a CPL conversion-controlled quick response (QR) code encryption system for the proof-of-concept imaging, as depicted in Figure 5b. Under the illumination of LCPL and RCPL at 3.88 mW cm^{-2}, the QR code mask is projected onto the device, and the photocurrent at each point is recorded. It can be clearly seen from the 3D histogram of current in the local area that the photocurrent generated under LCPL illumination is higher than that under RCPL illumination, which appears as a brighter light blue in the light mapping. 2D current map images are obtained by extracting the photocurrent values. While no significant features are visible under RCPL illumination, switching the light source to LCPL enables the encrypted QR code to be fully visualized and read directly by a smartphone. These results underscore the potential of our 2D chiral perovskite-based CPL detector for information encryption applications, which accelerates the practical application of CPL detection technology.

3. Conclusion

In summary, highly chiral 2D perovskites are obtained through a tailored achiral-chiral cation mixing strategy. Using a specific amount of achiral cation with lower steric hindrance, we can adjust the interlayer spacing and the degree of orientational order. Experimental results and crystallographic studies confirm the chiral transfer mechanism mediated by intermolecular interactions and tilting of the inorganic framework. The enhanced chirality and in-plane transport endow the CPL detector based on this material with the highest g_{Iph} among chiral 2D perovskite-based self-powered CPL detectors. Moreover, the excellent CPL detection performance enables the device to exhibit high-fidelity visualization and outstanding resolution, thus achieving encrypted information transmission. This work demonstrates that the tailored achiral-chiral cation mixing in 2D perovskites is an effective strategy for amplifying the chiral effect and can develop high-performance CPL photodetectors for potential applications such as CPL-sensitive imaging systems and information encryption.

4. Experimental Section

Details of the experiments and methods are provided in the Supporting Information.

Supporting Information

Supporting Information is available from the Wiley Online Library or from the author.

Acknowledgements

This work is supported by the National Natural Science Foundation of China (Nos. 52425308, 62204047, 62374035, and 92263106).

Conflict of Interest

The authors declare no conflict of interest.

Author Contributions

Y.R.G., X.S.F., and Z.Q.L. conceived the idea and designed the experiments. Y.R.G. conducted the experiments and wrote the manuscript under the supervision of X.S.F. and Z.Q.L. M.D. processed the GIWAXS data, contributed to data analysis and assisted in writing the manuscript. X.Y.Z. and Y.H. participated in fabricating the device and analyzed the data. L.S. supported with material characterization and optoelectronic measurements. All authors contributed to the work and commented on the paper.

Data Availability Statement

All data generated or analyzed during this study, along with its Supplementary Information, are included in this published article and are also available from the corresponding authors upon reasonable request. The crystal structures generated in this study have been deposited in the Cambridge Crystallographic Data Center under accession codes CCDC: 2365736 and 2365737 and can be obtained free of charge from the CCDC via https://www.ccdc.cam.ac.uk/structures/.

Keywords

2D perovskite, chirality, circularly polarized light, information encryption, photodetector

Received: June 12, 2025
Revised: July 13, 2025
Published online: July 31, 2025

[1] J. Crassous, M. J. Fuchter, D. E. Freedman, N. A. Kotov, J. Moon, M. C. Beard, S. Feldmann, *Nat. Rev. Mater.* **2023**, *8*, 365.
[2] J. Dong, Y. Liu, Y. Cui, *Nat. Chem.* **2024**, *16*, 1398.
[3] Y. Dang, X. Liu, B. Cao, X. Tao, *Matter* **2021**, *4*, 794.
[4] J. Ma, H. Wang, D. Li, *Adv. Mater.* **2021**, *33*, 2008785.
[5] Z. Q. Li, T. Yan, X. S. Fang, *Nat. Rev. Mater.* **2023**, *8*, 587.
[6] X. Zhang, Z. Q. Li, E. Hong, T. Yan, X. S. Fang, *Adv. Mater.* **2025**, *37*, 2412014.
[7] Y. Hu, X. Zhang, X. Mo, J. Chu, X. S. Fang, Z. Q. Li, *Adv. Funct. Mater.* **2025**, *35*, 2412015.
[8] T. Duan, Y. Zhou, *Adv. Energy Mater.* **2022**, *13*, 2200792.
[9] J. Son, G. Jang, S. Ma, H. Lee, C. U. Lee, S. Yang, J. Lee, S. Moon, W. Jeong, J. H. Park, J. Kim, D. H. Kim, J. S. Park, J. Moon, *Adv. Funct. Mater.* **2024**, *34*, 2413041.
[10] H. Wang, L. Yao, Y. Zhan, H. Yu, S. Wu, X. Liu, *ACS Appl. Mater. Interfaces* **2025**, *17*, 3716.
[11] Y. Xie, J. Morgenstein, B. G. Bobay, R. Song, N. A. M. S. Caturello, P. C. Sercel, V. Blum, D. B. Mitzi, *J. Am. Chem. Soc.* **2023**, *145*, 17831.
[12] Z. Zhang, W. Liang, J. Xue, X. Li, K. Wu, H. Lu, *ACS Nano* **2024**, *18*, 5890.
[13] J. Wu, X. Zhang, S. You, Z. K. Zhu, T. Zhu, Z. Wang, R. Li, Q. Guan, L. Liang, X. Niu, J. Luo, *Small* **2023**, *19*, 2302443.
[14] T. Duan, S. You, M. Chen, W. Yu, Y. Li, P. Guo, J. J. Berry, J. M. Luther, K. Zhu, Y. Zhou, *Science* **2024**, *384*, 878.
[15] X. Zhang, Y. Xu, A. N. Alphenaar, S. Ramakrishnan, Y. Zhang, A. J. Babatunde, Q. Yu, *ACS Nano* **2024**, *18*, 14605.
[16] S. You, P. Yu, T. Zhu, Q. Guan, J. Wu, H. Dai, H. Zhong, Z.-K. Zhu, J. Luo, *Mater. Horiz.* **2023**, *10*, 5307.
[17] Z. K. Zhu, T. Zhu, S. You, P. Yu, J. Wu, Y. Zeng, Y. Jiang, X. Liu, L. Li, C. Ji, J. Luo, *Adv. Sci.* **2023**, *11*, 2307593.
[18] T. Zhu, H. Wu, C. Ji, X. Zhang, Y. Peng, Y. Yao, H. Ye, W. Weng, W. Lin, J. Luo, *Adv. Opt. Mater.* **2022**, *10*, 2200146.
[19] S. Yang, G. Jang, C. U. Lee, J. Son, J. Lee, W. Jeong, D. G. Roe, J. H. Cho, J. Moon, *Adv. Funct. Mater.* **2024**, *34*, 2310917.
[20] J. Ahn, E. Lee, J. Tan, W. Yang, B. Kim, J. Moon, *Mater. Horiz.* **2017**, *4*, 851.
[21] A. Ben-Moshe, A. Teitelboim, D. Oron, G. Markovich, *Nano Lett.* **2016**, *16*, 7467.
[22] J. Son, S. Ma, Y.-K. Jung, J. Tan, G. Jang, H. Lee, C. U. Lee, J. Lee, S. Moon, W. Jeong, A. Walsh, J. Moon, *Nat. Commun.* **2023**, *14*, 3124.
[23] H. Song, M. Kwak, W. Choi, D. Yoo, J. H. Oh, *Adv. Opt. Mater.* **2024**, *12*, 2401427.
[24] J. Hu, X. Wen, D. Yang, Y. Chen, Z. Liu, D. Li, *Nano Lett.* **2024**, *24*, 1001.
[25] A. Dibenedetto, C. Coccia, M. Boiocchi, M. Moroni, C. Milanese, L. Malavasi, *J. Phys. Chem. C* **2024**, *128*, 4803.
[26] S. Ma, J. Ahn, J. Moon, *Adv. Mater.* **2021**, *33*, 2005760.
[27] W. Wu, Q. Chen, J. Cao, J. Fu, Z. Zhang, L. Chen, D. Rui, J. Zhang, Y. Zhou, B. Song, *ACS Appl. Mater. Interfaces* **2024**, *16*, 16340.
[28] Z. Guo, J. Li, R. Liu, Y. Yang, C. Wang, X. Zhu, T. He, *Nano Lett.* **2023**, *23*, 7434.
[29] C. U. Lee, S. Ma, J. Ahn, J. Kyhm, J. Tan, H. Lee, G. Jang, Y. S. Park, J. Yun, J. Lee, J. Son, J.-S. Park, J. Moon, *J. Am. Chem. Soc.* **2022**, *144*, 16020.

© 2025 Wiley-VCH GmbH

18638899, 2025, 24, Downloaded from https://onlinelibrary.wiley.com/doi/10.1002/lpor.202501468 by Fudan University, Wiley Online Library on [09/03/2026]. See the Terms and Conditions (https://onlinelibrary.wiley.com/terms-and-conditions) on Wiley Online Library for rules of use; OA articles are governed by the applicable Creative Commons License

[30] W. Wu, X. Shang, Z. Xu, H. Ye, Y. Yao, X. Chen, M. Hong, J. Luo, L. Li, *Adv. Sci.* **2023**, *10*, 2206070.
[31] E. Hong, Z. Q. Li, X. Zhang, X. Fan, X. S. Fang, *Adv. Mater.* **2024**, *36*, 2400365.
[32] Y. Jin, F. Lu, D. Yi, J. Li, F. Zhang, T. Sheng, F. Zhan, Y. Duan, G. Huang, J. Dong, B. Zhou, X. Wang, J. Yao, *CCS Chem.* **2021**, *3*, 1453.
[33] X. Fu, T. He, S. Zhang, X. Lei, Y. Jiang, D. Wang, P. Sun, D. Zhao, H.-Y. Hsu, X. Li, M. Wang, M. Yuan, *Chem* **2021**, *7*, 3131.
[34] Y. Shao, W. Gao, H. Yan, R. Li, I. Abdelwahab, X. Chi, L. Rogée, L. Zhuang, W. Fu, S. P. Lau, S. F. Yu, Y. Cai, K. P. Loh, K. Leng, *Nat. Commun.* **2022**, *13*, 138.
[35] F. Zeng, W. Kong, Y. Liang, F. Li, Y. Lvtao, Z. Su, T. Wang, B. Peng, L. Ye, Z. Chen, X. Gao, J. Huang, R. Zheng, X. Yang, *Adv. Mater.* **2023**, *35*, 2306051.
[36] Z. Han, W. Fu, Y. Zou, Y. Gu, J. Liu, B. Huang, D. Yu, F. Cao, X. Li, X. Xu, H. Zeng, *Adv. Mater.* **2021**, *33*, 2003852.
[37] R. Ollearo, A. Caiazzo, J. Li, M. Fattori, A. J. J. M. van Breemen, M. M. Wienk, G. H. Gelinck, R. A. J. Janssen, *Adv. Mater.* **2022**, *34*, 2205261.
[38] M. Qin, P. F. Chan, X. Lu, *Adv. Mater.* **2021**, *33*, 2105290.
[39] Y. Zhang, Y. Wang, X. Yang, L. Zhao, R. Su, J. Wu, D. Luo, S. Li, P. Chen, M. Yu, Q. Gong, R. Zhu, *Adv. Mater.* **2021**, *34*, 2107420.
[40] H. Tsai, W. Nie, J.-C. Blancon, C. C. Stoumpos, R. Asadpour, B. Harutyunyan, A. J. Neukirch, R. Verduzco, J. J. Crochet, S. Tretiak, L. Pedesseau, J. Even, M. A. Alam, G. Gupta, J. Lou, P. M. Ajayan, M. J. Bedzyk, M. G. Kanatzidis, A. D. Mohite, *Nature* **2016**, *536*, 312.
[41] Y. Yang, C. Liu, A. Mahata, M. Li, C. Roldán-Carmona, Y. Ding, Z. Arain, W. Xu, Y. Yang, P. A. Schouwink, A. Züttel, F. De Angelis, S. Dai, M. K. Nazeeruddin, *Energy Environ. Sci.* **2020**, *13*, 3093.
[42] S. Li, X. Liu, H. Yang, H. Zhu, X. S. Fang, *Nat. Electron.* **2024**, *7*, 216.
[43] Z. Zhao, C. Xu, Y. Ma, K. Yang, M. Liu, X. Zhu, Z. Zhou, L. Shen, G. Yuan, F. Zhang, *Adv. Funct. Mater.* **2022**, *32*, 2203606.
[44] X. Zhao, K. Yang, X. Ma, M. H. Jee, H. Qu, S. Zhang, Y. Ma, L. Shen, G. Yuan, Q. Yao, H. Y. Woo, F. Zhang, *Chem. Eng. J.* **2025**, *517*, 164473.
[45] M. Deng, Z. Q. Li, S. Liu, X. S. Fang, L. Wu, *Nat. Commun.* **2024**, *15*, 8789.
[46] X. Jia, R. Guo, B. K. Tay, X. Yan, *Adv. Funct. Mater.* **2022**, *32*, 2205933.
[47] W. R. Kitzmann, J. Freudenthal, A. P. M. Reponen, Z. A. VanOrman, S. Feldmann, *Adv. Mater.* **2023**, *35*, 2302279.
[48] H. Ye, Y. Peng, M. Wei, X. Zhang, T. Zhu, Q. Guan, L. Li, S. Chen, X. Liu, J. Luo, *Chem. Mater.* **2023**, *35*, 6591.
[49] G. Long, R. Sabatini, M. I. Saidaminov, G. Lakhwani, A. Rasmita, X. Liu, E. H. Sargent, W. Gao, *Nat. Rev. Mater.* **2020**, *5*, 423.
[50] A. Maiti, A. J. Pal, *Angew. Chem., Int. Ed.* **2022**, *61*, 202214161.
[51] P. J. Huang, K. Taniguchi, M. Shigefuji, T. Kobayashi, M. Matsubara, T. Sasagawa, H. Sato, H. Miyasaka, *Adv. Mater.* **2021**, *33*, 2008611.
[52] X. Wang, Y. Wang, W. Gao, L. Song, C. Ran, Y. Chen, W. Huang, *Adv. Mater.* **2021**, *33*, 2003615.

© 2025 Wiley-VCH GmbH

18638899, 2025, 24, Downloaded from https://onlinelibrary.wiley.com/doi/10.1002/lpor.202501468 by Fudan University, Wiley Online Library on [09/03/2026]. See the Terms and Conditions (https://onlinelibrary.wiley.com/terms-and-conditions) on Wiley Online Library for rules of use; OA articles are governed by the applicable Creative Commons License